









## Internal activities in a solar filament and heating to its threads

HENGYUAN WEI <sup>1</sup>, ZHENGHUA HUANG <sup>1</sup>, CHUAN LI <sup>2,3</sup>, ZHENYONG HOU <sup>4</sup>, YE QIU <sup>2,3</sup>, HUI FU <sup>1</sup>,  
XIANYONG BAI <sup>5</sup>, AND LIDONG XIA <sup>1</sup>

<sup>1</sup>*Shandong Key Laboratory of Optical Astronomy and Solar-Terrestrial Environment, Institute of Space Sciences, Shandong University, Weihai 264209, Shandong, China*

<sup>2</sup>*School of Astronomy and Space Science, Nanjing University, Nanjing 210023, China*

<sup>3</sup>*Key Laboratory for Modern Astronomy and Astrophysics (Nanjing University), Ministry of Education, Nanjing 210023, China*

<sup>4</sup>*School of Earth and Space Sciences, Peking University, Beijing, 100871, People's Republic of China*

<sup>5</sup>*National Astronomical Observatories, Chinese Academy of Sciences, Beijing, 100012, People's Republic of China*

### ABSTRACT

Filaments are one of the most common features in the solar atmosphere, and are of significance in solar, stellar and laboratory plasma physics. Using data from the Chinese H $\alpha$  Solar Explorer, the Solar Upper Transition Region Imager and the Solar Dynamics Observatory, we report on multiwavelength imaging and spectral observations of the activation of a small filament. The filament activation produces several localized dynamic brightenings, which are probably produced by internal reconnections of the braided magnetic fields in the filament. The filament expands during the activation and its threads reconnect with the ambient magnetic fields, which leads to the formation of hot arcades or loops overlying the filament. The thermal energy of each of these localized brightenings is estimated in the order of  $10^{25} - 10^{27} \text{erg}$  and the total energy is estimated to be  $\sim 1.77 \times 10^{28} \text{erg}$ . Our observations demonstrate that the internal magnetic reconnections in the filament can lead to localized heating to the filament threads and prompt external reconnections with ambient corona structures, and thus could contribute to the energy and mass transferring into the corona.

*Keywords:* Sun: atmosphere—Sun: corona—Sun: filament—magnetic reconnection—methods: data analysis

### 1. INTRODUCTION

Filaments, also called prominences while appearing at the limb, are common features in the solar atmosphere with dense, cool and partially ionized plasma. They anchor to the photosphere with anti-polarity, extend along the polarity inversion lines (PILs) and outward to the hot corona. They could be unambiguously observed in chromospheric lines such as H $\alpha$  and EUV passbands such as 304 Å and 171 Å (Parenti 2014). The instabilities and eruptions of filaments could lead to solar flares and/or coronal mass ejections (Chen 2011; Shibata & Magara 2011; Shen et al. 2012a; Benz 2017; Shen et al. 2019a). Thanks to the high-resolution facilities, more and more fine structures are reported, which show complex dynamics in the filament and raise much more puzzles about the phenomenon (Gibson 2018).

Filaments are formed in filament channels along the PILs (Martin 1998; Mackay et al. 2010) and the chromospheric filamentary threads are aligned with the filament channels, whose magnetic structures are thought to be sheared-arcades or twisted flux-ropes (Amari et al. 1999; DeVore & Antiochos 2000; Fan & Gibson 2004; Gibson & Fan 2006; Aulanier et al. 2002). Many studies have demonstrated that numbers of eruptive filament events are associated with internal reconnection and thus internal reconnection plays an important role in filament associated activities. Moore et al. (2001) observed magnetic explosion events with flares and coronal mass ejections (CMEs), and the internal reconnection of filaments is crucial in the onset and growth of these eruptive events. Sterling & Moore (2004) reported that the external and internal reconnections cause the eruption of the filament-carrying magnetic cavity. Shen et al.

(2012b) reported that the external and internal reconnection of filament could produce simultaneously bubble-like and jet-like CME. Gary & Moore (2004) illustrated that the external reconnection leads to the internal reconnection of filament, which releases the helix and heats a two-ribbon flare. Tripathi et al. (2009) found that most partial eruptions of prominences could be explained by partially-expelled-flux-rope model which is associated with internal reconnection. Cheng et al. (2018) suggested that the splitting of filament involving internal reconnection could induce eruptions of filament. Huang et al. (2018) suggested that the free magnetic energy could be released into upper atmosphere through reconnection process. Many observations and simulations indicated that the internal reconnection of filaments or mini-filaments could trigger jets in the corona (Sterling et al. 2015; Panesar et al. 2016; Wyper et al. 2017; Shen et al. 2017, 2019b; Wei et al. 2022).

Many complex motions, small-scale filament-eruption-like features and fine structures in filament are also widely reported in previous literatures. Shen et al. (2015) indicated that the magnetic reconnection at separator could cause upflows and this could intrude into downflow area and form counter-streaming mass flows. Sterling et al. (2020) reported several small-scale eruptions of sub-minifilaments which could be caused by magnetic reconnections or acoustic waves. Li et al. (2023) studied the event of mini-filament and found that the mini-filament eruption experiences both internal and external reconnection, which transfers mass and flux to ambient corona. Tiwari et al. (2019) found brightenings at the ends of loops in an arch filament system, which lie on the opposite-polarity magnetic convergence, and these brightenings are likely caused by magnetic cancellation. Chen et al. (2020) found a series of coronal mini-jets in an activated tornado-like prominence, and these mini-jets were thought to be the results of fine-scale external or internal reconnections between the prominence magnetic field and background field or the twisted or braided fields in the prominence. Li et al. (2022b) demonstrated that the repeated, intermittent small-scale  $H\alpha$ /EUV bursts at the same place were related to the growth of the filament channel. Huang et al. (2019) reported several localized brightenings in filament in microwaves with a temporal variations of 3-5 s, which correspond to the EUV bright threads, fibers or spots, and these brightenings might be caused by internal reconnection or electric field acceleration. Zhou et al. (2016) reported some brightenings in the lengthening and widening process of filament, these brightenings form at the interface between different short and thin threads and are the results of reconnection among those threads.

In this paper, we report on multiwavelength imaging and spectroscopic observations of the activation of a filament. In this case, the activated filament is confined with a series of localized small-scale brightenings, and results in overlying hot arcades. We will investigate in-depth how these small-scale localized brightenings form and the thermal and dynamic evolution of the filament. In what follows, we give the data description in Section 2, results in Section 3, discussion in Section 4 and conclusions in Section 5.

## 2. OBSERVATIONS

The data were observed on 2022 November 1 from 16:50 UT to 17:15 UT with a target of AR 13135, by the space-borne Atmospheric Imaging Assembly (AIA, Lemen et al. 2012) and the Helioseismic and Magnetic Imager (HMI, Scherrer et al. 2012) onboard the Solar Dynamics Observatory (SDO, Pesnell et al. 2012), the  $H\alpha$  Imaging Spectrograph (HIS, Liu et al. 2022) onboard the Chinese  $H\alpha$  Solar Explorer (CHASE, Li et al. 2022a; Zhang et al. 2022) and the Solar Upper Transition Region Imager (SUTRI, Bai et al. 2023; Wang et al. 2023).

The data analyzed involve the line-of-sight magnetograms observed by HMI, images taken by the AIA EUV passbands of 94, 131, 171, 193, 211, 304 and 335 Å, images with SUTRI at Ne VII 465 Å and the spectral data of  $H\alpha$  and Fe I lines with HIS.

The AIA data have a pixel size of 0.6'' with a cadence of 12 s for EUV images and 24 s for 1600 Å images. The HMI data have a pixel size of 0.6'' and a cadence of 45 s. Both AIA and HMI data are reduced by the standard procedure of *aia\_prep.pro* in solarsoft.

The HIS was running in a ‘‘Raster Scanning Mode’’ (RSM) to obtain spectra of the full solar disk. A full-disk scanning takes about 60 seconds. The present dataset includes 10 rasters of the full-disk obtained from 16:45:04 UT to 16:55:42 UT. The spatial resolution of the binning mode data used in this paper is 1.04''/pixel, while the spectral resolution is 0.048 Å/pixel. We analyze the spectral data of  $H\alpha$  (6559.7 - 6565.9 Å) and Fe I (6567.8 - 6570.6 Å) in this study. The latter one is applied to co-align with the AIA and HMI observations. The production of spectral data is level 1 after full calibrations (Qiu et al. 2022).

The SUTRI images have a spatial resolution of 1.23''/pixel and 30 s cadence. It observes the Sun at Ne VII 465 Å whose formation temperature is around 0.5 MK (Tian 2017). The data production downloaded is high-level scientific data which have been fully calibrated by the instrument team.

The images from different passbands and instruments have been aligned by the reference structures (such as sunspots, filaments and networks) in the passbands with the closest representative temperatures.

### 3. RESULTS

The event occurs on the disk from 16:50 to 17:15 UT and the overview of this event is shown in Figure 1. A filament with a length of around 71 arcsec can be unambiguously observed in HIS  $H\alpha$  passband and AIA 304 Å and 171 Å passbands (see the red dash lines in panel a). This filament extends along the PIL and connects the positive polarity P1 and negative polarity N1 (see panel c), which indicates that the magnetic configuration of the filament is a normal-polarity topology (Chen et al. 2014). At around 16:51:29 UT, the filament activation begins to occur, with the brightening of an arcade (hereafter A1) overlying the filament (see white arrows in panels d-f). After that the filament destabilizes and starts to activate, several localized brightenings appear in most AIA EUV passbands and SUTRI 465 Å passband (see the blue arrows in panels h and i). In addition, during the process of activation, the filament expands obviously, leading to the appearance of two brightenings at both sides of the filament at around 17:00:11 UT, with an unidirectional flow towards east end of the filament appearing (see brightenings pointed by green arrows in panel g). It is followed by the formation of hot arcades overlying the filament (hereafter called A2), which can be only observed in AIA 94 Å passband and connect the positive polarity P1 and negative polarity N2 (see the blue dash lines in panel c and red dash lines in panel l).

Before the activation of the filament at 16:51:29 UT, we observe the arcade A1 overlying the filament with a small loop nearby in the observation of AIA 304 Å passband (marked with the green and cyan dash lines in panel (a) in Figure 2 respectively). At 16:51:53 UT, the interface between the A1 and small loop brightens, forming a new post-reconnected bright arcade overlying the filament and a post-reconnected small loop marked by green and cyan dash lines in panel (b) in Figure 2. After this process, the first localized brightening appears at the place pointed by a yellow arrow in panel (c) in Figure 2 while the filament threads near the east footpoint start to split (see the blue arrows in panel (c) in Figure 2). At 16:55:17 UT, another arcade (hereafter called A3) overlying the filament marked with white dash line in panel (d) in Figure 2 brightens, and the filament threads near the east footpoint continue splitting during this period (blue arrows in panel (d) in Figure 2). Later, more localized brightenings appear after destabilization of the filament. With the boundary enhancement operator of *unsharp\_mask* in *ssw*, we are able to trace several bright threads of the filament in the enhanced AIA 171 Å passband images (see the red lines in Figure 6 (a)). We find that the localized brightenings are located on the threads and some of them are located at the cross section of these bright threads. At 16:56:05 UT, a series of brightenings appear near the east footpoint of the filament, and they seem to have different locations while seen on different AIA EUV passbands (see the diamonds with different colors in panel (e) in Figure 2).

To study the dynamics of the localized brightenings on the filament, we make the slice-time plot along a slit along the filament (see red dash lines in panels (g) and (i) in Figure 1). In Figure 3, we find that the dynamics of these localized brightenings shows similar trend in both AIA 171 Å passband and SUTRI 465 Å passband. Some localized brightenings stay still (see the blue arrows in panel (a)-(b)) while some others propagate along the filament with speeds in the range of 50–70 km/s (see the green dash lines). The stationary localized brightenings appear prior to those propagating localized brightenings. Furthermore, some still localized brightenings occur at the same place repeatedly.

Using the  $H\alpha$  spectral data from CHASE, we obtain the dopplergram of the region of interest with the moment method (Yu et al. 2020). The reference spectrum is obtained from the average of those in the field-of-view shown in Figure 1(b). At 16:47:27 UT, we observe that some red shifted regions with speeds at around 1 km/s emerge at the places marked (see black contours in panel (b)-(d) in Figure 4) and the sizes of these red shifted regions seem to expand after 16:53:20 UT, when the first localized brightening appears. These red shifted regions are located next to the localized brightenings in AIA EUV passbands (see the green contours in panel (d) in Figure 4). We further investigate the evolution of the average spectral profiles in three red shifted structures marked with rectangles with L1, L2 and L3 in panel (d) of Figure 4. We can see that the  $H\alpha$  profiles in these regions are red-shifted in prior to the event (see the spectral profiles in Figure 5 at 16:45:04 UT and 16:47:27 UT). During the event,  $H\alpha$  profiles show deeper blue wings and line centers while the red wings are almost not affected (see the spectral profiles in Figure 5 at 16:54:33 UT and 16:55:42 UT), although the whole profiles are remaining red-shifted. The red shift of  $H\alpha$  centroid might suggest the sinking of the filament and internal energy release. While the blue-wing absorption indicates the injection of filament materials or the upward motion of filament materials. The Ti II 6559.5 Å and Si I 6560.6 Å seem to be not affected by the event, except in the cases where the far blue wing of  $H\alpha$  profile is strongly affected.



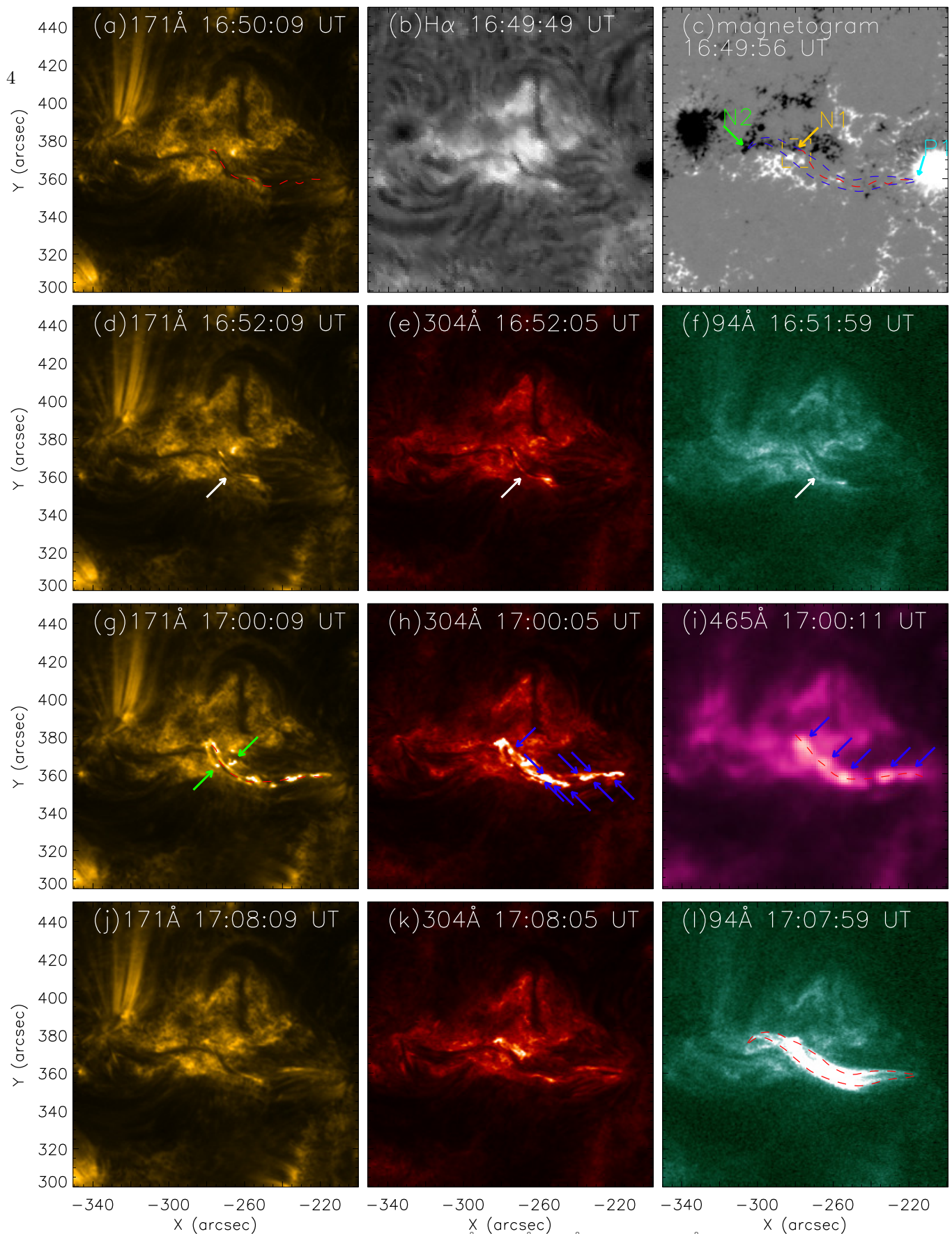


**Figure 1.** Overview of the region of interest in AIA 171 Å, 304 Å, 94 Å, SUTRI 465 Å, HIS  $H\alpha$  and HMI line-of-sight magnetogram. (a): The red dash line outlines the shape of the filament. (c): The cyan arrow marked as P1 points to the positive polarity of the filament and arcade A2, the yellow arrow marked as N1 points to the negative polarity of the filament and the green arrow marked as N2 points to the negative polarity of the arcade A2. The red dash line resembles the trajectory of the filament and the blue dash lines resemble the trajectory of the arcade A2. (d)-(f): The white arrows point to the bright arcade A1 overlying the filament. (g): The green arrows point to the brightenings associated with the formation of the arcade A2. The red dash line shows the trajectory that obtains the slice-time plot. (h)-(i): The blue arrows point to the localized brightenings. The red dash line in (i) shows the trajectory that obtains the slice-time-plot. (l): The red dash lines show the trajectory of the arcade A2. An associated animation is available online. The animation shows the evolution of this region in these passbands from 16:50:11 UT to 17:49:47 UT. The real-time duration of the animation is 30 s.

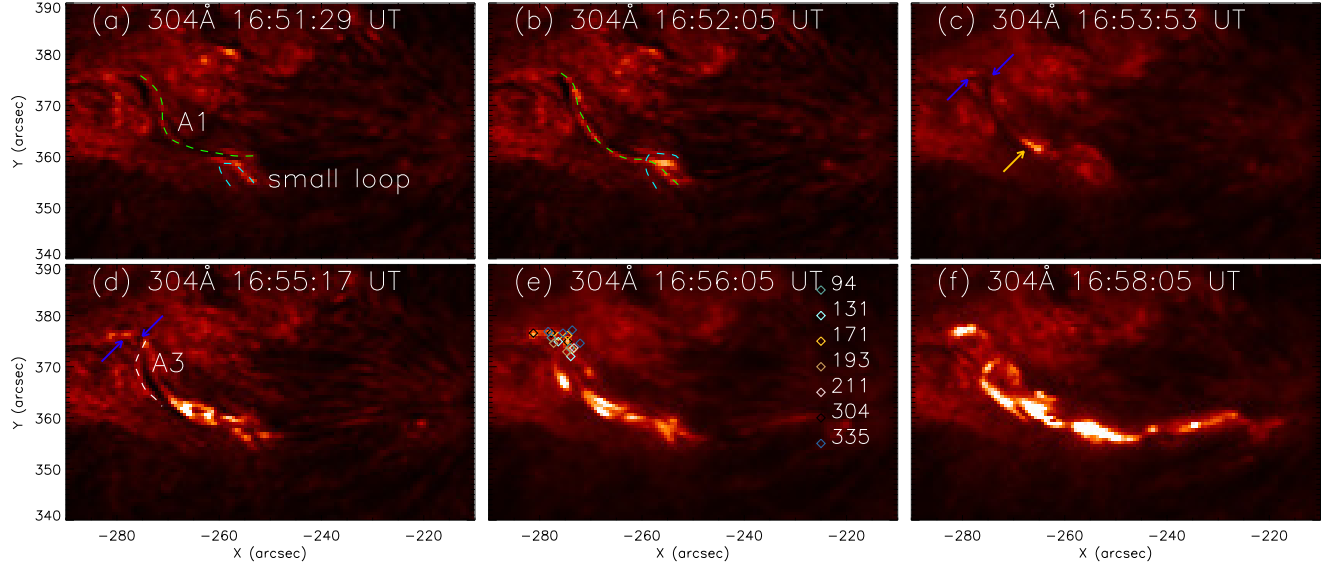


**Figure 2.** The triggering process of the filament activation in AIA 304 Å from 16:51:29 UT to 16:58:05 UT. (a): The snapshot of AIA 304 Å observation at 16:51:29 UT, the green dash line marks the position of an arcade overlying the filament and the cyan dash line marks a nearby loop. (b): The snapshot of AIA 304 Å observation at 16:52:05 UT, the green and cyan dash lines mark the arcade and loop after reconnection. (c): The snapshot of AIA 304 Å observation at 16:53:53 UT, the blue arrows point to the eastern filament footpoint which begins to split. The yellow arrow points to the first localized brightening. (d): The snapshot of AIA 304 Å observation at 16:55:17 UT, the blue arrows point to the eastern filament footpoint which has splitted, and the white dash line marks another brightened arcade. (e): The snapshot of AIA 304 Å observation at 16:56:05 UT, the diamonds in different colours resemble the the position of bright points near the eastern footpoint of filament in AIA 94, 131, 171, 193, 211, 304, 335 passbands. (f): The snapshot of AIA 304 Å observation at 16:58:05 UT.

To investigate the thermal dynamics and density evolution of this region, we apply differential emission measure (DEM) analysis (Cheung et al. 2015; Su et al. 2018) based on the observations taken by AIA 94, 131, 171, 193, 211 and 335 Å passbands and get the emission measure (EM) of the region. Using the EM data, we inverse the weight-average temperature and density distribution and evolution of this area with Equations 1,

$$\begin{aligned}
 EM &= \int DEM(T) dT, \\
 \bar{T} &= \frac{\int DEM(T) \times T dT}{\int DEM(T) dT}, \\
 n &= \sqrt{\frac{EM}{L}},
 \end{aligned} \tag{1}$$

where DEM is the differential emission measure, T is the temperature and L is the depth/width of the structures along line-of-sight (Cheng et al. 2012). Here, we use the width of filament to estimate the accurate density of filament. Before activation of the filament, the arcade A1 overlying the filament shows a temperature at around  $\log(T/K) = 6.6$  and already shows a weak density enhancement. During the activation process, the temperature response first enhances at the middle part of the filament with the highest temperatures given at the localized brightenings, while the density increase starts from the east end of the filament and spreads toward the west (see the associated animation of Figure 6). The localized brightenings appear in a wide range of temperature from  $\log(T/K) = 5.5$  to  $\log(T/K) = 7.3$  and the average temperature is estimated to be over  $8 \times 10^6$  K. The filament is heated to near  $8 \times 10^6$  K during the activation process. The arcades A2 overlying the filament, which can be only observed in AIA 94 Å passband, have a strong EM response in  $\log(T/K) = 6.7-7.0$  and are cooled down in tens of minutes after the activation, which is shown as the disappearance of bright structure in AIA 94 Å. The average temperature of these arcades A2 is around  $\log(T/K) = 6.7-6.8$  (see associated animation of Figure 6).

#### 4. DISCUSSION

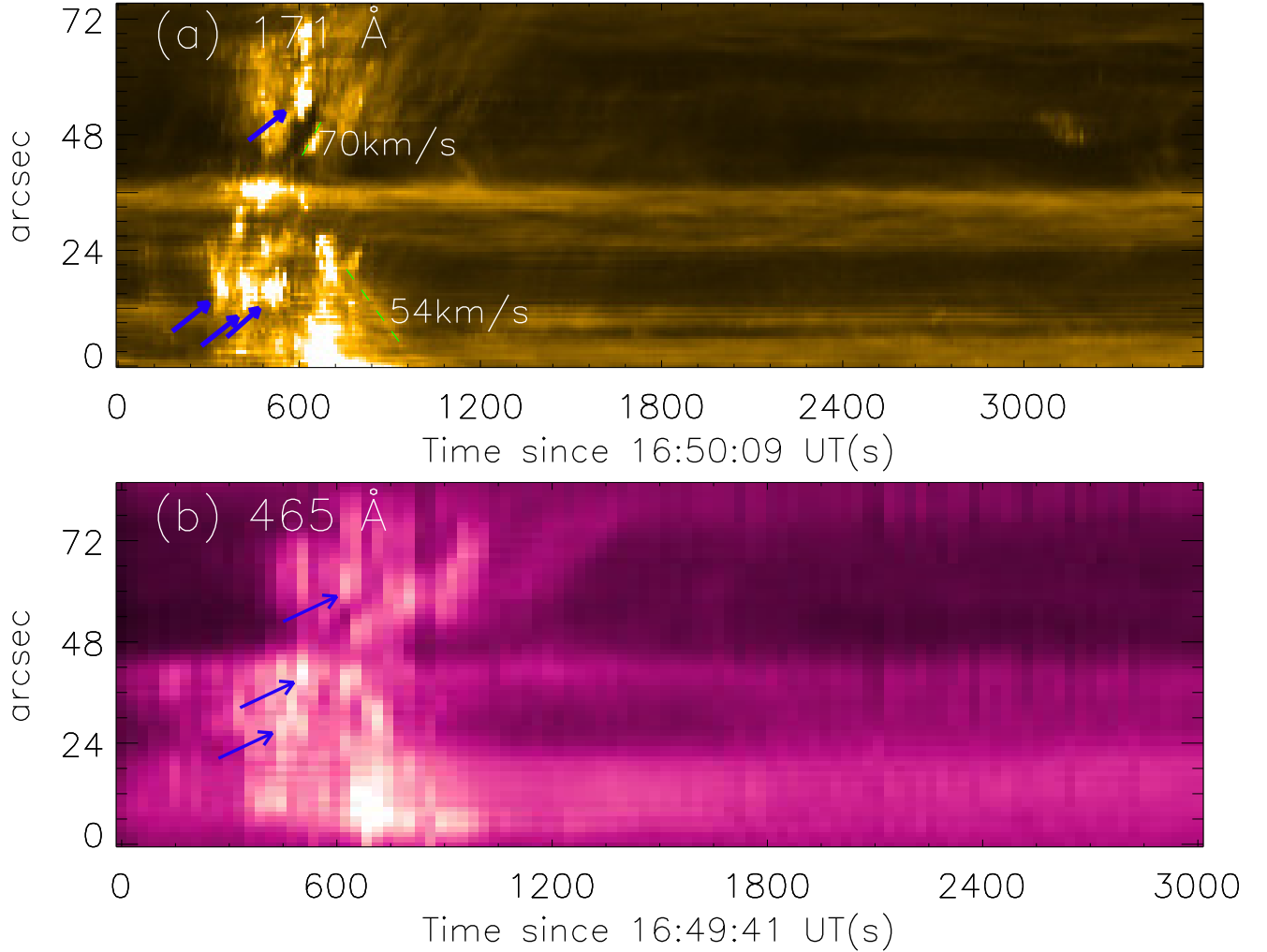


**Figure 3.** Slice-time plot along the red dash lines in Figure 1 (g) and (i). The blue arrows in panel (a) and (b) point to several still localized brightenings. The green dash lines in panel (a) trace some moving brightenings.

Based on the observations, we analyze the triggering process of activation and possible reasons for the localized brightenings in the filament. Using the statistic results reported by [Chen et al. \(2014\)](#) and [Ouyang et al. \(2017\)](#) and the magnetic configuration observed by HMI, which is normal-polarity, we can determine that the magnetic structure of the filament more likely consists of magnetic dips with arcades above.

Before the onset of the activation, the brightened arcade A1 overlying the filament (marked with green dash line in panel (a) in Figure 2) rises and reconnects with a nearby small loop (marked with cyan dash line in panel (a) in Figure 2), producing brightening at the interface between the small loop and A1 and forming new post-reconnected arcade and small loop (see green and cyan dash lines in panel (b) in Figure 2). This reconnection process destabilizes the filament, leading to the sinking of filament threads which is shown as the expansion of red shifted region in the dopplergrams (see the black contours in Figure 4). We observe that there exists small misalignment between the localized red shifted regions and localized brightenings (see green contours in panel (d) in Figure 4), indicating that the internal reconnections occur among the magnetic field lines with dips supporting the filament threads, rather than among the filament threads. The sinking of filament threads promotes the internal reconnection between different field lines that support the filament, which might have been braided before the activation, producing the first localized brightening in the filament (see the yellow arrow in panel (c) in Figure 2). The evolution of spectral profiles in the red shifted regions shows deeper blue wings and line centers during the event (see Figure 5), suggesting that some filament threads are rising whilst materials are filling in. During the activation process, the material of filament threads might move along the magnetic dips upwards, which is also manifested as the deeper blue wings of spectral profiles. Furthermore,



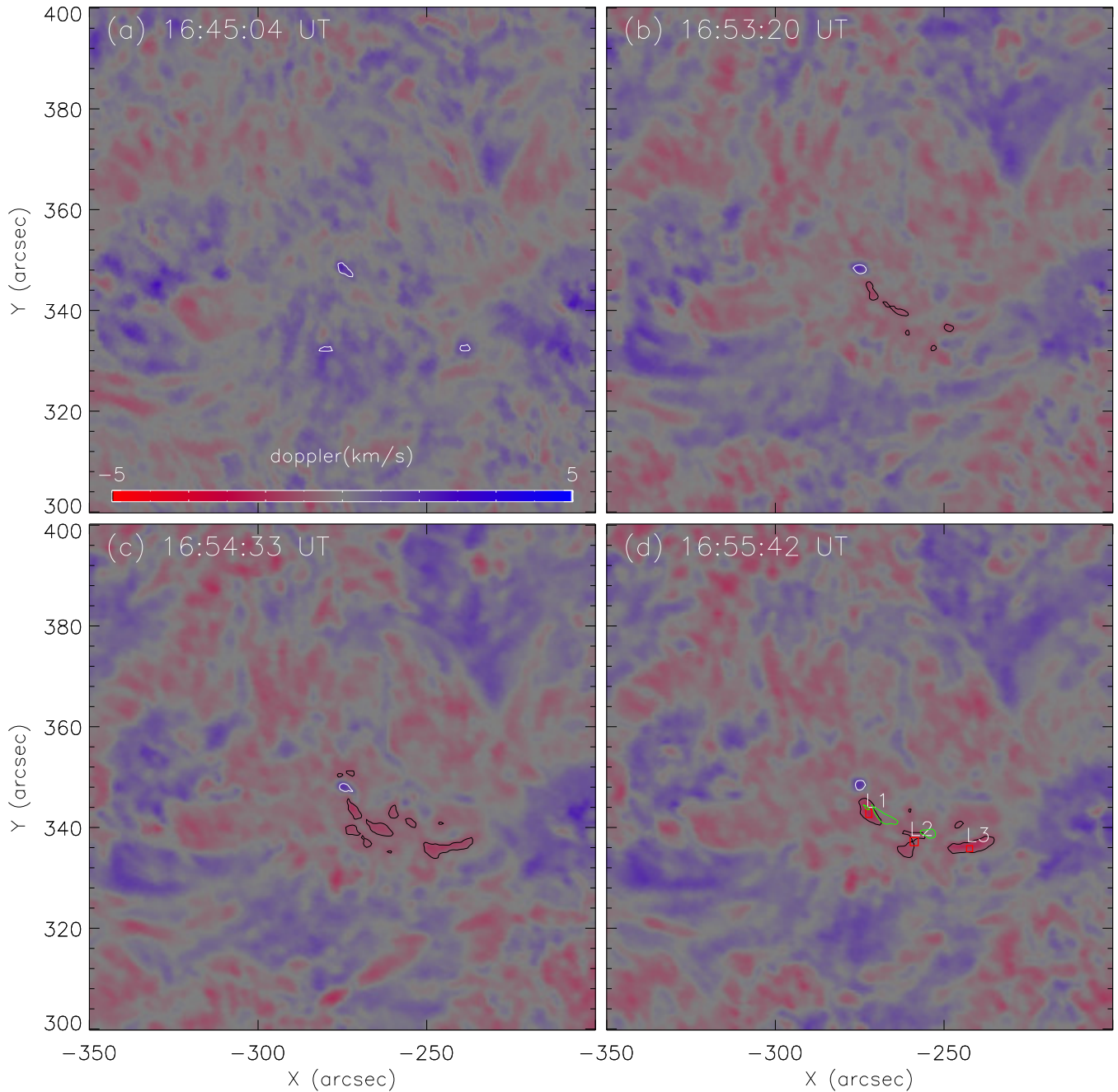


**Figure 4.** Dopplergrams of the region of interest in the wavelength of  $H\alpha$ . (a)-(d): The dopplergrams in 16:45:04 UT, 16:53:20 UT, 16:54:33 UT and 16:55:42 UT. The white lines contour the blue shift at the level of 1 km/s. The black lines in panel (b)-(d) show the contours of red shift at the level of 0.8 km/s. The red rectangles marked with L1, L2, L3 show the positions where we obtain the spectral profiles shown in figure 5. The green contours in panel (d) mark the localized brightenings in AIA 171 Å on 16:55:45 UT at a level of 3000 DN.

destabilization of the filament causes split of the filament threads near the east footpoint (see the blue arrows in panel (c) and (d) in Figure 2), which further increases destabilization of the filament. During this process, the other arcade A3 overlying the filament brightens (see the white dash line in panel (d) in Figure 2) and a series of bright points appear near the east footpoint of the filament, which lie on different locations in different AIA EUV passbands (see diamonds in panel (e) in Figure 2). These bright points may resemble the footpoints of arcades overlying the filament

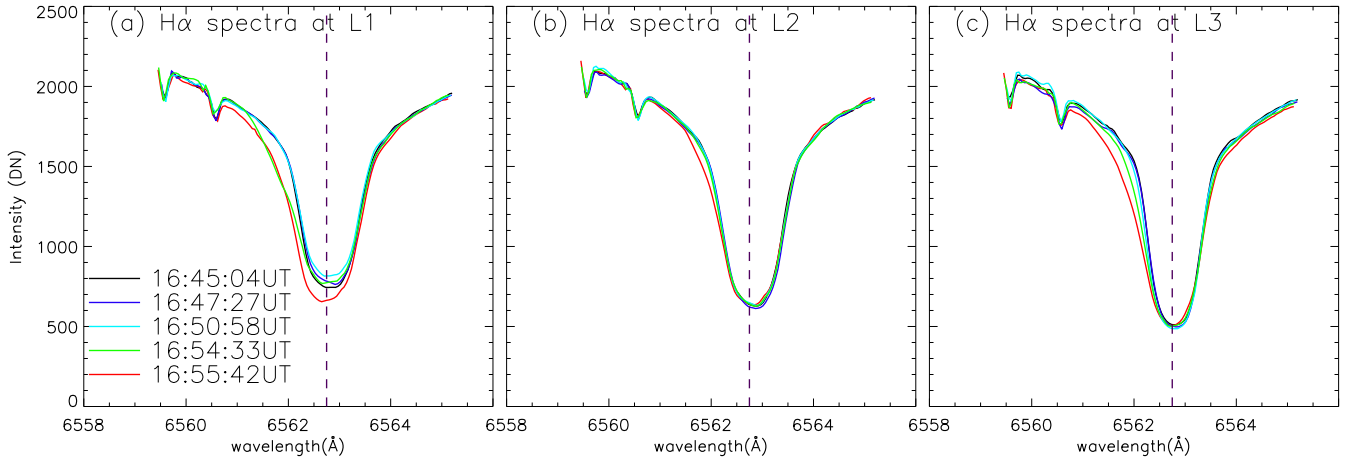


**Figure 5.** Evolution of the spectral profiles at the red shift regions marked as L1, L2, L3 in Figure 4. The black, blue, cyan, green and red lines in panels (a)-(c) show the spectral profiles at L1, L2 and L3 at 16:45:04 UT, 16:47:27 UT, 16:50:58 UT, 16:54:33 UT and 16:55:42 UT. The purple dash line represents the position of line core of reference spectral profile.

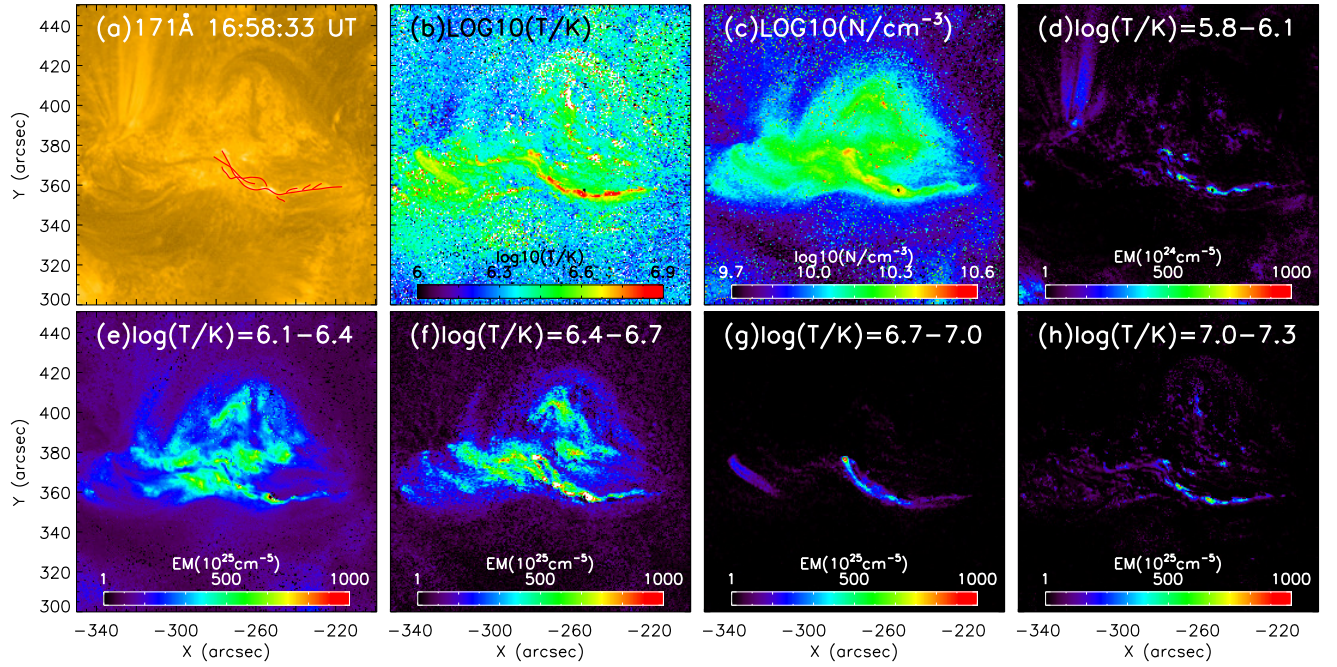


**Figure 6.** Differential emission measure of the region of interest. (a): The enhanced logarithm image with `unsharp_mask` operator in AIA 171 Å in 16:58:53 UT. The red lines mark the trajectory of the brightened threads of filament. (b): The weighted temperature distribution of the region. (c): The density distribution of the region. (d)-(h): The emission measure of the region in the range of  $\log(T/K) = 5.8-7.3$ . An associated animation of this area is available online. The animation includes the evolution of the region seen in AIA 171 Å, temperature distribution and density distribution from 16:49:59 UT to 17:43:59 UT. The real-time duration of the animation is 30 s.

which are lightened during the activation process and may promote the internal reconnections between different field lines. Numerous localized brightenings appear in the filament as a result of a series of internal reconnections. Parts of these localized brightenings are located at the cross-sections of different filament threads (see the red lines in panel (a) in Figure 6), again indicating that these localized brightenings are related to internal reconnections among different field lines that support the filament.

Through the slice-time plots along the filament in AIA 171 Å passband and SUTRI, we find that a few localized brightenings stay still (see the blue arrows in Figure 3) while some others propagate along the filament threads with



a speed of 50-70 km/s (see the green dash lines in Figure 3). These stationary localized brightenings appear prior to the moving brightenings, and we believe they are caused by the heating effects of internal reconnections. Some stationary localized brightenings occur at the same place several times (see the three bottom blue arrows in panel (a) in Figure 3), which indicates that the internal reconnections occur at the same place repeatedly, and this could play an important role in coronal heating as reported by Cheng et al. (2023). For those moving brightenings, their size, multi-thermal nature, speed and density are similar to those found in jets and multi-flux-rope system (Zhang & Ji 2014; Shen 2021; Awasthi et al. 2018). These moving brightenings are multi-thermal with temperatures in the range of  $\log(T/K) = 5.5-7.3$ , and their lifetimes, intensity enhancement in relative to the background are several minutes and 0.7-0.8, respectively. These parameters suggest that they are likely to be the plasmoids or blobs produced in the internal reconnection processes by the tearing-mode instability (Wyper et al. 2016; Zhang & Ni 2019). Prior & Yeates (2016a,b) compared the behaviour of twisted and braided magnetic field through simulations, and they found that during eruption processes the twisted magnetic fields turn to sigmoid with obvious global rotation while the braided magnetic fields expand significantly without global rotation. In this event, we obviously observe expansion of the filament during its activation process, which indicates that the magnetic field lines hosting the magnetic dips may be highly braided before the activation.

In the later activation process, at 17:00:11 UT, brightenings at both sides of the filament (see green arrows in panel (g) in Figure 1) appear, followed by the unidirectional flow towards eastern footpoint of the filament. After these bright points and flow, the arcades A2 overlying the filament which can be only observed in AIA 94 Å passband form. During the expansion of the filament, some filament threads encounter background magnetic fields, forming current sheet at their interface, which is shown as brightenings at both sides of the filament. This process is followed by the external reconnections between the filament threads and background magnetic fields, and the unidirectional flow is parts of the outflow of reconnection. The reconnection process causes the formation of post-reconnected arcades A2 overlying the filaments (see the blue dash lines in panel (c) and red dash lines in panel (l) in Figure 1) and heats them to extremely high temperature, which can interpret that the arcades A2 can only be observed in AIA 94 Å passband. This indicates that the internal reconnections of the filament promote the occurrence of external reconnections between the filament threads and nearby background magnetic field. After the activation, the filament cools down in tens of minutes, shown as the gradual disappearance of bright structure in AIA 94 Å passband, which is in the same order of radiative cooling time scale in the corona (Rosner et al. 1978; Reale 2014).

Using the DEM inversion method from Cheng et al. (2012), we obtain the distributions of weight-averaged temperature and density. Furthermore, we estimate the widths of the filament and several localized brightenings by fitting the intensity distributions of their cross-sections with Gaussian functions (see the width given in Figure 7). The width of the filament is about  $2.4 \times 10^8$  cm while those of the localized brightenings are  $9.0 \times 10^7$  cm,  $7.1 \times 10^7$  cm,  $5.3 \times 10^7$  cm,  $1.6 \times 10^8$  cm and  $1.2 \times 10^8$  cm, respectively. The initial temperature and density are  $3 \times 10^6$  K and  $2 \times 10^{10}$  cm<sup>-3</sup>, respectively, while the temperature and density at their peaks are  $8 \times 10^6$  K and  $2.8 \times 10^{10}$  cm<sup>-3</sup>, respectively. As we obtain the parameters of spatial size, temperature and density, we could estimate the thermal energy ( $E$ ) of the active filament threads and localized brightenings via  $E = 3N_e k_B T V$ , where  $N_e$ ,  $k_B$ ,  $T$  and  $V$  are the electron number density, Boltzmann constant, temperature and volume, respectively (Tian et al. 2014; Chen et al. 2020; Hou et al. 2021). We could estimate the volume of filament with  $V = \frac{1}{4}\pi d^2 L$  where  $d$  is the width of the filament and  $L$  is the length of the filament and the volume of the localized brightenings with  $V = \frac{4}{3}\pi r^3$  where  $r$  is the radius of brightenings. The total energy that heats the filament is about  $1.77 \times 10^{28}$  erg and the energy that each of the localized brightenings produces is in the order of  $10^{25} - 10^{27}$  erg, which is in the same order of microflares (Hudson 1991; Krucker & Benz 1998; Aschwanden et al. 2000; Parnell & Jupp 2000; Hannah et al. 2011).

According to the observations above, we give a scenario to interpret these processes in Figure 8. The black ovals marked with plus and minus symbols indicate the positive and negative polarities, and the black dash line represents the position of the PIL. The red line in panel (a) represents the ambient magnetic field. Before activities of the filament, the filament threads, marked with orange ovals, are supported by magnetic field lines hosting magnetic dips (green and blue lines) with overlying arcades (purple lines). The purple and yellow lines in panel (a) mark the arcades overlying the filament and nearby small loop respectively. Firstly, the arcade reconnects with nearby small loop, which destabilizes the filament, leading to the sinking of the filament threads. The blue and green lines in panel (b) indicate different magnetic field lines supporting filament threads. Some of these magnetic lines may be braided before activation of the filament. The sinking of filament threads promotes the internal reconnections between different magnetic field lines hosting magnetic dips, which then result in brightenings of the footpoints of the

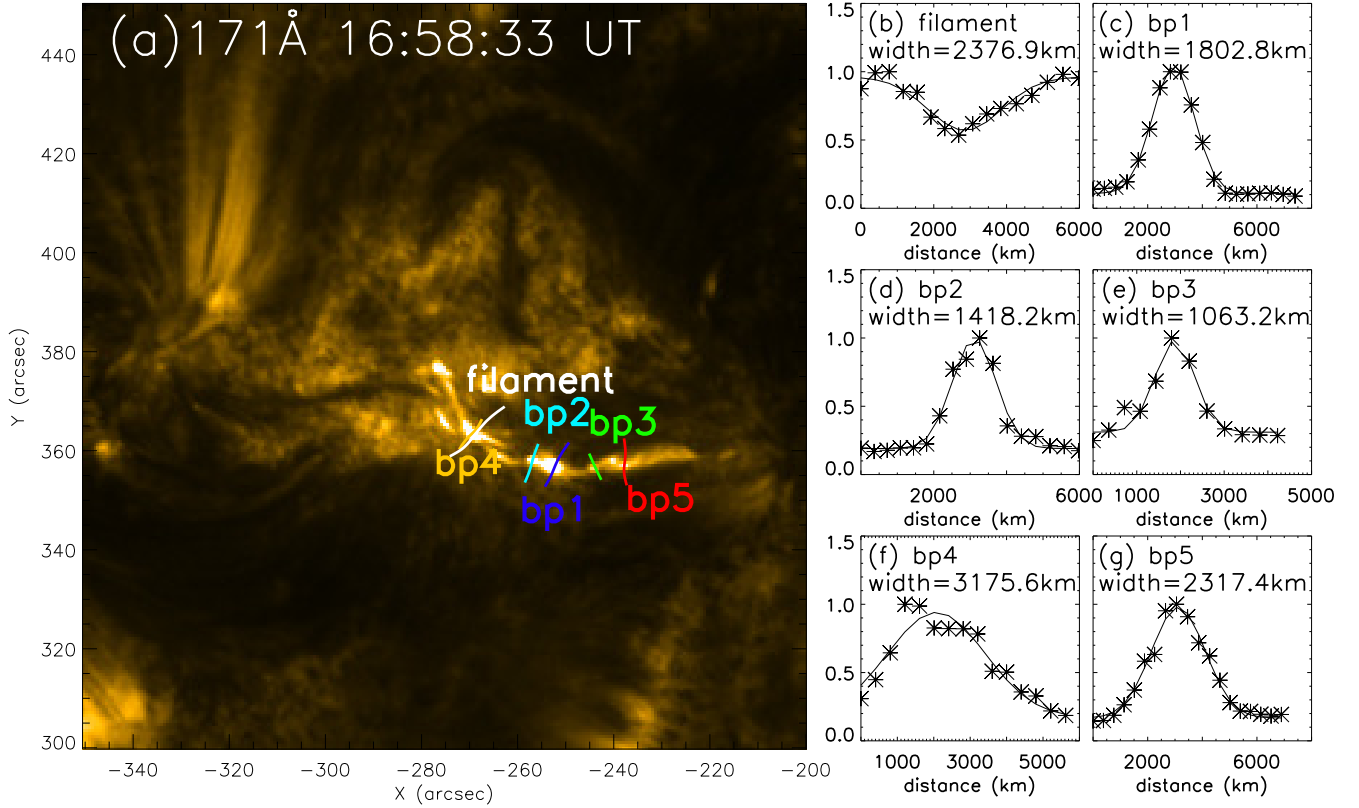


**Figure 7.** Estimation of the width of filament and several localized brightenings. (a): The image observed in AIA 171 Å in 16:58:33 UT. The white line resembles the position where we estimate the width of the filament. The blue, cyan, green, yellow and red lines resemble the position where we estimate the width of localized brightenings. (b)-(g): The dotted lines show the intensity distributions along the trajectory in panel (a). The black lines show the gaussfit results.

arcades overlying the filament (see the blue arrows in panel (c) and (d)). Series of localized brightenings are produced in these internal reconnection processes with some being stationary and others propagating along post-reconnected arcades. The stationary brightenings are caused by the heating effects of internal reconnection while the propagating brightenings could be the blobs or plasmoids caused by tearing-mode instability (Wyper et al. 2016; Zhang & Ni 2019). The internal reconnections are accompanied by the expansion of the filament, and this promotes the external reconnection between the filament threads and background magnetic fields (see panel (e)). The arcades A2 which can be only observed in AIA 94 Å passband, marked by brown line in panel (f), form in these external reconnection process.

## 5. CONCLUSION

In this paper, we report on an eruptive event of a filament with a length of about 70 arcsec observed by SDO, CHASE and SUTRI. The magnetic geometry of this filament consists of magnetic fields hosting magnetic dips with arcades overlying them. The activation of the filament can be divided into three stages: 1) the triggering process when the arcades overlying the filament reconnect with ambient loops; 2) internal reconnection process when a series of localized brightenings appear in the filament; 3) external reconnection process when the arcades A2 form.

Before the activation of the filament (stage 1), the arcade A1 overlying the filament brightens and reconnects with a nearby small loop, forming new post-reconnected arcade and loop, which destabilizes the filament and promotes the onset of internal reconnection between different magnetic field lines hosting magnetic dips. The first localized brightening appears at the middle of filament, located near the localized red-shifted region seen in HIS H $\alpha$  spectral data. This indicates that this brightening is caused by internal reconnection between the magnetic field lines supporting the filament threads. The blue wings of spectral profiles in red shifted region deepen during the activation process, and this indicates some threads may rise after the internal reconnection or materials are injected into the filament. During this process, the filament threads at its east footpoint begin to split, which further destabilizes the filament and

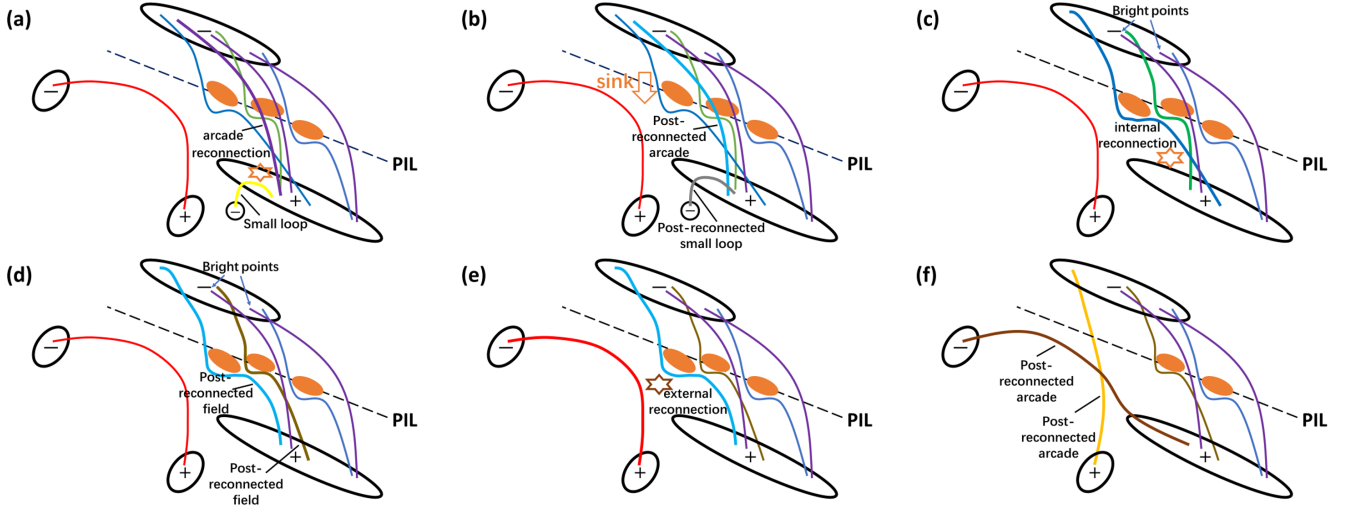


**Figure 8.** A scenario interpreting the reconnection process in this event. (a): The initial magnetic structures. The green and blue lines resemble the magnetic field lines hosting dips and supporting the filament threads which are shown by orange ovals. The purple lines mark the arcades overlying the filament. The yellow line is the small loop nearby. The red line shows background magnetic field. (b): The time after reconnection between arcade and nearby loop. The grey and cyan lines mark the post-reconnected loop and arcade respectively. (c): The internal reconnection between different magnetic field lines hosting dips. (d): The time after internal reconnection. The cyan and gold lines mark the post-reconnected arcades. (e): The external reconnection. (f): The time after external reconnection. The brown line marks the arcade A2 only observed in AIA 94 Å passband and the yellow line shows another post-reconnected arcade.

promotes the occurrence of internal reconnections. Meanwhile, numerous bright points appear adjacent to the east footpoint of the filament and their locations differ in different AIA EUV passbands. These bright points are related to the footpoints of the arcades overlying the magnetic field lines hosting magnetic dips, which may be engaged into the activation process.

In the activation process (stage 2), the filament expands obviously, which is similar to the evolution of braided magnetic field simulated by (Prior & Yeates 2016a,b), demonstrating that the magnetic field lines hosting dips may be braided before the activation. Series of localized brightenings appear in the filament and can be observed in most AIA EUV passbands and SUTRI 465 Å passband. These localized brightenings are located at the filament threads and some of them lie at the cross section of different filament threads, which indicates that these localized brightenings are related to the internal reconnections. Through the slice-time plot along the filament, we find that some localized brightenings are stationary, which are caused by the heating effects of the internal reconnections among magnetic field lines hosting magnetic dips, while others move with speeds ranging from 50 km/s to 70 km/s. These moving brightenings have similar size, multi-thermal nature, speed and density with the blobs or plasmoids in jets and multi-flux-rope system (Zhang & Ji 2014; Shen 2021; Awasthi et al. 2018), though there exist some differences in their lifetime, intensity enhancement relative to background and temperature range. So these moving brightenings are likely to be the blobs or plasmoids produced in the internal reconnection process by tearing-mode instability (Wyper et al. 2016; Zhang & Ni 2019). These localized brightenings show a wide temperature range at  $\log(T/K) = 5.5-7.3$ , and the weight-averaged temperature is estimated over  $8 \times 10^6 K$ . Some filament threads are heated to  $8 \times 10^6 K$  from  $3 \times 10^6 K$  after series of brightenings. The total energy released in this heating process is estimated to be  $1.77 \times 10^{28} \text{erg}$  and the energy each brightening provided is in the range of  $10^{25} - 10^{27} \text{erg}$ , which is in the same order of microflares (Hudson 1991; Krucker & Benz 1998; Aschwanden et al. 2000; Parnell & Jupp 2000; Hannah et al. 2011).

The filament expands obviously during its activation process, and we observe bright points at both sides of the filament in the stage 3 (see the green arrows in Figure 1 (g)), followed by an unidirectional flow towards the eastern footpoint of the filament. These bright points may be the places where the filament threads reconnect with ambient magnetic field while the flow is part of the outflow of external reconnection. After these external reconnections, arcades A2 overlying the filament which can be only observed in AIA 94 Å appear. This demonstrates that the internal reconnection in the activation process can promote the expansion of filament and drive the occurrence of external reconnection.



*Acknowledgement:* We are grateful to the anonymous referee for the constructive comments. This research is supported by National Key R&D Program of China No. 2021YFA0718600 and National Natural Science Foundation of China (42230203, 42174201, 41974201, 12333009). CHASE mission is supported by China National Space Administration. SUTRI is a collaborative project conducted by the National Astronomical Observatories of CAS, Peking University, Tongji University, Xi'an Institute of Optics and Precision Mechanics of CAS and the Innovation Academy for Microsatellites of CAS. The AIA and HMI data are used by courtesy of NASA/SDO, the AIA and HMI teams and JSOC.

## REFERENCES

- Amari, T., Luciani, J. F., Mikic, Z., & Linker, J. 1999, ApJL, 518, L57, doi: [10.1086/312053](https://doi.org/10.1086/312053)
- Aschwanden, M. J., Tarbell, T. D., Nightingale, R. W., et al. 2000, ApJ, 535, 1047, doi: [10.1086/308867](https://doi.org/10.1086/308867)
- Aulanier, G., DeVore, C. R., & Antiochos, S. K. 2002, ApJL, 567, L97, doi: [10.1086/339436](https://doi.org/10.1086/339436)
- Awasthi, A. K., Liu, R., Wang, H., Wang, Y., & Shen, C. 2018, ApJ, 857, 124, doi: [10.3847/1538-4357/aab7fb](https://doi.org/10.3847/1538-4357/aab7fb)
- Bai, X., Tian, H., Deng, Y., et al. 2023, Research in Astronomy and Astrophysics, 23, 065014, doi: [10.1088/1674-4527/accc74](https://doi.org/10.1088/1674-4527/accc74)
- Benz, A. O. 2017, Living Reviews in Solar Physics, 14, 2, doi: [10.1007/s41116-016-0004-3](https://doi.org/10.1007/s41116-016-0004-3)
- Chen, H., Zhang, J., De Pontieu, B., et al. 2020, ApJ, 899, 19, doi: [10.3847/1538-4357/ab9cad](https://doi.org/10.3847/1538-4357/ab9cad)
- Chen, P. F. 2011, Living Reviews in Solar Physics, 8, 1, doi: [10.12942/lrsp-2011-1](https://doi.org/10.12942/lrsp-2011-1)
- Chen, P. F., Harra, L. K., & Fang, C. 2014, ApJ, 784, 50, doi: [10.1088/0004-637X/784/1/50](https://doi.org/10.1088/0004-637X/784/1/50)
- Cheng, X., Kliem, B., & Ding, M. D. 2018, ApJ, 856, 48, doi: [10.3847/1538-4357/aab08d](https://doi.org/10.3847/1538-4357/aab08d)
- Cheng, X., Zhang, J., Saar, S. H., & Ding, M. D. 2012, ApJ, 761, 62, doi: [10.1088/0004-637X/761/1/62](https://doi.org/10.1088/0004-637X/761/1/62)
- Cheng, X., Priest, E. R., Li, H. T., et al. 2023, Nature Communications, 14, 2107, doi: [10.1038/s41467-023-37888-w](https://doi.org/10.1038/s41467-023-37888-w)
- Cheung, M. C. M., Boerner, P., Schrijver, C. J., et al. 2015, ApJ, 807, 143, doi: [10.1088/0004-637X/807/2/143](https://doi.org/10.1088/0004-637X/807/2/143)
- DeVore, C. R., & Antiochos, S. K. 2000, ApJ, 539, 954, doi: [10.1086/309275](https://doi.org/10.1086/309275)
- Fan, Y., & Gibson, S. E. 2004, ApJ, 609, 1123, doi: [10.1086/421238](https://doi.org/10.1086/421238)
- Gary, G. A., & Moore, R. L. 2004, ApJ, 611, 545, doi: [10.1086/422132](https://doi.org/10.1086/422132)
- Gibson, S. E. 2018, Living Reviews in Solar Physics, 15, 7, doi: [10.1007/s41116-018-0016-2](https://doi.org/10.1007/s41116-018-0016-2)
- Gibson, S. E., & Fan, Y. 2006, Journal of Geophysical Research (Space Physics), 111, A12103, doi: [10.1029/2006JA011871](https://doi.org/10.1029/2006JA011871)
- Hannah, I. G., Hudson, H. S., Battaglia, M., et al. 2011, SSRv, 159, 263, doi: [10.1007/s11214-010-9705-4](https://doi.org/10.1007/s11214-010-9705-4)
- Hou, Z., Tian, H., Berghmans, D., et al. 2021, ApJL, 918, L20, doi: [10.3847/2041-8213/ac1f30](https://doi.org/10.3847/2041-8213/ac1f30)
- Huang, J., Tan, B., Masuda, S., et al. 2019, ApJ, 874, 176, doi: [10.3847/1538-4357/ab0e80](https://doi.org/10.3847/1538-4357/ab0e80)
- Huang, Z., Mou, C., Fu, H., et al. 2018, ApJL, 853, L26, doi: [10.3847/2041-8213/aaa88c](https://doi.org/10.3847/2041-8213/aaa88c)
- Hudson, H. S. 1991, SoPh, 133, 357, doi: [10.1007/BF00149894](https://doi.org/10.1007/BF00149894)
- Krucker, S., & Benz, A. O. 1998, ApJL, 501, L213, doi: [10.1086/311474](https://doi.org/10.1086/311474)
- Lemen, J. R., Title, A. M., Akin, D. J., et al. 2012, SoPh, 275, 17, doi: [10.1007/s11207-011-9776-8](https://doi.org/10.1007/s11207-011-9776-8)
- Li, C., Fang, C., Li, Z., et al. 2022a, Science China Physics, Mechanics, and Astronomy, 65, 289602, doi: [10.1007/s11433-022-1893-3](https://doi.org/10.1007/s11433-022-1893-3)
- Li, H. T., Cheng, X., Guo, J. H., et al. 2022b, A&A, 663, A127, doi: [10.1051/0004-6361/202243115](https://doi.org/10.1051/0004-6361/202243115)
- Li, Z. F., Cheng, X., Ding, M. D., et al. 2023, A&A, 673, A83, doi: [10.1051/0004-6361/202245814](https://doi.org/10.1051/0004-6361/202245814)
- Liu, Q., Tao, H., Chen, C., et al. 2022, Science China Physics, Mechanics, and Astronomy, 65, 289605, doi: [10.1007/s11433-022-1917-1](https://doi.org/10.1007/s11433-022-1917-1)
- Mackay, D. H., Karpen, J. T., Ballester, J. L., Schmieder, B., & Aulanier, G. 2010, SSRv, 151, 333, doi: [10.1007/s11214-010-9628-0](https://doi.org/10.1007/s11214-010-9628-0)
- Martin, S. F. 1998, SoPh, 182, 107, doi: [10.1023/A:1005026814076](https://doi.org/10.1023/A:1005026814076)
- Moore, R. L., Sterling, A. C., Hudson, H. S., & Lemen, J. R. 2001, ApJ, 552, 833, doi: [10.1086/320559](https://doi.org/10.1086/320559)
- Ouyang, Y., Zhou, Y. H., Chen, P. F., & Fang, C. 2017, ApJ, 835, 94, doi: [10.3847/1538-4357/835/1/94](https://doi.org/10.3847/1538-4357/835/1/94)
- Panesar, N. K., Sterling, A. C., Moore, R. L., & Chakrapani, P. 2016, ApJL, 832, L7, doi: [10.3847/2041-8205/832/1/L7](https://doi.org/10.3847/2041-8205/832/1/L7)
- Parenti, S. 2014, Living Reviews in Solar Physics, 11, 1, doi: [10.12942/lrsp-2014-1](https://doi.org/10.12942/lrsp-2014-1)
- Parnell, C. E., & Jupp, P. E. 2000, ApJ, 529, 554, doi: [10.1086/308271](https://doi.org/10.1086/308271)

- Pesnell, W. D., Thompson, B. J., & Chamberlin, P. C. 2012, *SoPh*, 275, 3, doi: [10.1007/s11207-011-9841-3](https://doi.org/10.1007/s11207-011-9841-3)
- Prior, C., & Yeates, A. R. 2016a, *A&A*, 591, A16, doi: [10.1051/0004-6361/201528053](https://doi.org/10.1051/0004-6361/201528053)
- . 2016b, *A&A*, 587, A125, doi: [10.1051/0004-6361/201527231](https://doi.org/10.1051/0004-6361/201527231)
- Qiu, Y., Rao, S., Li, C., et al. 2022, *Science China Physics, Mechanics, and Astronomy*, 65, 289603, doi: [10.1007/s11433-022-1900-5](https://doi.org/10.1007/s11433-022-1900-5)
- Reale, F. 2014, *Living Reviews in Solar Physics*, 11, 4, doi: [10.12942/lrsp-2014-4](https://doi.org/10.12942/lrsp-2014-4)
- Rosner, R., Tucker, W. H., & Vaiana, G. S. 1978, *ApJ*, 220, 643, doi: [10.1086/155949](https://doi.org/10.1086/155949)
- Scherrer, P. H., Schou, J., Bush, R. I., et al. 2012, *SoPh*, 275, 207, doi: [10.1007/s11207-011-9834-2](https://doi.org/10.1007/s11207-011-9834-2)
- Shen, Y. 2021, *Proceedings of the Royal Society of London Series A*, 477, 217, doi: [10.1098/rspa.2020.0217](https://doi.org/10.1098/rspa.2020.0217)
- Shen, Y., Liu, Y., Liu, Y. D., et al. 2015, *ApJL*, 814, L17, doi: [10.1088/2041-8205/814/1/L17](https://doi.org/10.1088/2041-8205/814/1/L17)
- Shen, Y., Liu, Y., & Su, J. 2012a, *ApJ*, 750, 12, doi: [10.1088/0004-637X/750/1/12](https://doi.org/10.1088/0004-637X/750/1/12)
- Shen, Y., Liu, Y., Su, J., & Deng, Y. 2012b, *ApJ*, 745, 164, doi: [10.1088/0004-637X/745/2/164](https://doi.org/10.1088/0004-637X/745/2/164)
- Shen, Y., Liu, Y. D., Su, J., Qu, Z., & Tian, Z. 2017, *ApJ*, 851, 67, doi: [10.3847/1538-4357/aa9a48](https://doi.org/10.3847/1538-4357/aa9a48)
- Shen, Y., Qu, Z., Zhou, C., et al. 2019a, *ApJL*, 885, L11, doi: [10.3847/2041-8213/ab4cf3](https://doi.org/10.3847/2041-8213/ab4cf3)
- Shen, Y., Qu, Z., Yuan, D., et al. 2019b, *ApJ*, 883, 104, doi: [10.3847/1538-4357/ab3a4d](https://doi.org/10.3847/1538-4357/ab3a4d)
- Shibata, K., & Magara, T. 2011, *Living Reviews in Solar Physics*, 8, 6, doi: [10.12942/lrsp-2011-6](https://doi.org/10.12942/lrsp-2011-6)
- Sterling, A. C., & Moore, R. L. 2004, *ApJ*, 613, 1221, doi: [10.1086/423297](https://doi.org/10.1086/423297)
- Sterling, A. C., Moore, R. L., Falconer, D. A., & Adams, M. 2015, *Nature*, 523, 437, doi: [10.1038/nature14556](https://doi.org/10.1038/nature14556)
- Sterling, A. C., Moore, R. L., Panesar, N. K., et al. 2020, *ApJ*, 889, 187, doi: [10.3847/1538-4357/ab5dcc](https://doi.org/10.3847/1538-4357/ab5dcc)
- Su, Y., Veronig, A. M., Hannah, I. G., et al. 2018, *ApJL*, 856, L17, doi: [10.3847/2041-8213/aab436](https://doi.org/10.3847/2041-8213/aab436)
- Tian, H. 2017, *Research in Astronomy and Astrophysics*, 17, 110, doi: [10.1088/1674-4527/17/11/110](https://doi.org/10.1088/1674-4527/17/11/110)
- Tian, H., Kleint, L., Peter, H., et al. 2014, *ApJL*, 790, L29, doi: [10.1088/2041-8205/790/2/L29](https://doi.org/10.1088/2041-8205/790/2/L29)
- Tiwari, S. K., Panesar, N. K., Moore, R. L., et al. 2019, *ApJ*, 887, 56, doi: [10.3847/1538-4357/ab54c1](https://doi.org/10.3847/1538-4357/ab54c1)
- Tripathi, D., Gibson, S. E., Qiu, J., et al. 2009, *A&A*, 498, 295, doi: [10.1051/0004-6361/200809801](https://doi.org/10.1051/0004-6361/200809801)
- Wang, Z., Yu, J., Qi, R., et al. 2023, *Research in Astronomy and Astrophysics*, 23, 095009, doi: [10.1088/1674-4527/ace17b](https://doi.org/10.1088/1674-4527/ace17b)
- Wei, H., Huang, Z., Fu, H., et al. 2022, *ApJ*, 936, 51, doi: [10.3847/1538-4357/ac85bf](https://doi.org/10.3847/1538-4357/ac85bf)
- Wyper, P. F., Antiochos, S. K., & DeVore, C. R. 2017, *Nature*, 544, 452, doi: [10.1038/nature22050](https://doi.org/10.1038/nature22050)
- Wyper, P. F., DeVore, C. R., Karpen, J. T., & Lynch, B. J. 2016, *ApJ*, 827, 4, doi: [10.3847/0004-637X/827/1/4](https://doi.org/10.3847/0004-637X/827/1/4)
- Yu, K., Li, Y., Ding, M. D., et al. 2020, *ApJ*, 896, 154, doi: [10.3847/1538-4357/ab9014](https://doi.org/10.3847/1538-4357/ab9014)
- Zhang, Q. M., & Ji, H. S. 2014, *A&A*, 567, A11, doi: [10.1051/0004-6361/201423698](https://doi.org/10.1051/0004-6361/201423698)
- Zhang, Q. M., & Ni, L. 2019, *ApJ*, 870, 113, doi: [10.3847/1538-4357/aaf391](https://doi.org/10.3847/1538-4357/aaf391)
- Zhang, W., Cheng, W., You, W., et al. 2022, *Science China Physics, Mechanics, and Astronomy*, 65, 289604, doi: [10.1007/s11433-022-1924-3](https://doi.org/10.1007/s11433-022-1924-3)
- Zhou, G., Wang, J., & Zhang, J. 2016, *SoPh*, 291, 2373, doi: [10.1007/s11207-016-0972-4](https://doi.org/10.1007/s11207-016-0972-4)